Wideband, Electrically Small, Near-Field Resonant Parasitic Dipole Antenna with Stable Radiation Performance

Xiaoming Chen, *Student Member, IEEE*, Ming-Chun Tang, *Senior Member, IEEE*, Da Yi, *Member, IEEE*, and Richard W. Ziolkowski, *Life Fellow, IEEE*

***Abstract*—A wideband, electrically small, near-field resonant parasitic (NFRP) dipole antenna with stable radiation performance is presented. Inspired by recent metasurface antennas, a coax-fed dipole antenna is loaded with a specially-engineered interdigitated NFRP element. It exhibits identical operating mechanisms to a developed electrically large slot-fed metasurface antenna, i.e., it has the similar adjacent fundamental mode and anti-phase mode, and thus has a wide bandwidth property and uniform radiation patterns. The electrically small prototype was fabricated and measured. The measured results, in good agreement with their simulated values, demonstrate a wide 14.4% -10-dB impedance bandwidth along with a stable realized gain of 1.4 dBi over the entire band. Moreover, stable and uniform radiation patterns together with high radiation efficiency values were also measured. These performance characteristics make the reported ESA attractive for wideband and space-limited applications.**

***Index Terms*—Dipole antennas, electrically small antennas, interdigitated structures, metasurface antennas, near-field resonant parasitic antennas.**

I. Introduction

ELECTRICALLY small antennas (ESAs) generally suffer from narrow bandwidths (Chu limit [1]) and low radiation efficiencies, which hinder their applications in many wireless systems. It continues to be a challenge to realize one antenna exhibiting the advantageous features of compactness, high radiation efficiency (RE) and wide bandwidth at the same time. Near-field resonant parasitic (NFRP) ESAs have recently drawn considerable attention as a potential solution. Their merits include high radiation efficiency, easy fabrication, and good matching to a source without any external feeding network [2]-[5]. Many effective methods have been adopted in order to increase their narrow operating bandwidths. They can be classified generally into two categories: passive and active. The passive ones employ multiple NFRP elements with several adjacent overlapping resonances to achieve a wider bandwidth [6]-[9], while the active approaches integrate non-Foster elements into the radiators [10], [11].

Metasurface antennas (MSAs) [12]-[18] have been reported recently that have the attractive characteristics of being low profile and having wide operational bandwidths. A close collaboration between their periodic patches and aperture coupling feed facilitates the excitation of dual resonant modes, i.e., a TM_{10} mode and an antiphase TM_{20} mode [13]. Therefore, a broad impedance bandwidth and stable boresight radiation patterns are obtained over the entire operational frequency range.

Inspired by the MSA designs, a NFRP ESA is developed in this Letter that has a significantly expanded impedance bandwidth without utilizing multiple NFRP elements or active elements. A patch-based NFRP dipole antenna is first examined that has a resonance mechanism analogous to a MSA. An electrically small version is then attained using an interdigitated NFRP structure. This miniaturization is realized without deteriorating the bandwidth or RE values. A prototype was fabricated and tested. The measured results, in agreement with their simulated values, indicate that this ESA provides a stable realized gain, ~1.4 dBi, over the entire fractional bandwidth ~14.4%. The prototype is electrically small with its $ka \sim 0.987$, where $k = 2\pi/\lambda_0 = 2\pi f_L/c$ is the corresponding free-space wavenumber, f_L is the lower bound of the operational band, and a is the radius of the smallest sphere that completely encloses the entire antenna system.

II. MSA-Inspired NFRP Dipole Antenna

A. Design

The MSA design derived from the concepts in [13] is shown in Fig. 1(a). The corresponding MSA-inspired NFRP dipole antenna is displayed in Fig. 1(b). The substrates employed in the design are all Rogers RO4003C, whose dielectric constant is $\varepsilon_r = 3.38$ and loss tangent is $\tan\delta = 0.0027$. The MSA is driven by a narrow slot in the ground plane that is excited by an

Manuscript received on 8th, February, 2020; revised on 12th, March, 2020; accepted on 14th, March, 2020.

This work was supported in part by the National Natural Science Foundation of China contract number 61922018; the Graduate Scientific Research and Innovation Foundation of Chongqing, China contract number CYS18062; the Funding of the leading research talent cultivation plan of Chongqing University contract number cqu2017hbrc1A08; the Chongqing Natural Science Foundation contract number cstc2019jcyjjqX0004; and in part by the Australian Research Council grant number DP160102219. (*Corresponding author: Ming-Chun Tang.*)

X. Chen, M.-C. Tang, and D. Yi are with the Key Laboratory of Dependable Service Computing in Cyber Physical Society Ministry of Education, College of Communication Engineering, Chongqing University, Chongqing 400044, China (E-mail: tangmingchun@cqu.edu.cn).

R. W. Ziolkowski is with the University of Technology Sydney, Global Big Data Technologies Centre, Ultimo NSW 2007, Australia (E-mail: Richard.Ziolkowski@uts.edu.au).

orthogonal microstrip feedline. It has a 4×4 metal patch-based metasurface printed on the top surface of its substrate, which is 4.5 mm thick. In contrast, the NFRP antenna is driven by a simple center-fed (gap-excited) dipole. No metal ground is present. The substrate's transverse size is the same, but it is only 2.0 mm thick. A 4×1 array of metal patches acts as a NFRP structure. The driven dipole is located immediately beneath and is parallel to the patch array.

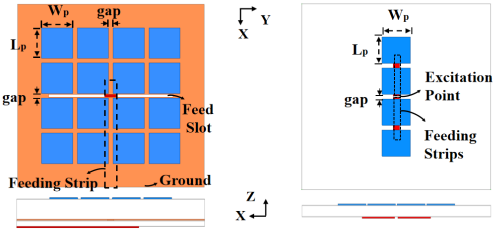

Fig. 1. Top view and lateral view of the initial two antenna. (a) Slot-fed MSA. (b) Gap-excited NFRP dipole antenna.

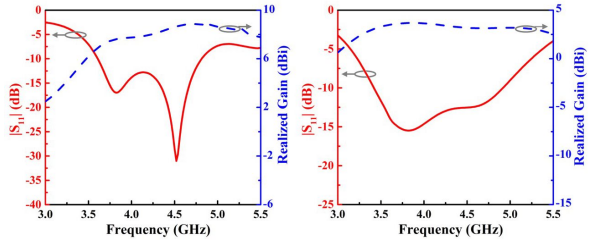

Fig. 2. Simulated $|S_{11}|$ and realized gain values of the antennas as functions of the source frequency. (a) Slot-fed MSA. (b) Gap-excited NFRP dipole antenna.

The radiating patches in both antennas have the same dimensions: $W_p \times L_p$=10.2 mm×10.0 mm. The gaps between the patches are also the same: *gap* = 1.0 mm. The corresponding simulated reflection coefficients ($|S_{11}|$) together with the realized gain values of both antennas are displayed in Figs. 2(a) and (b). One clearly sees that two adjacent resonant modes in each case overlap to produce the wide operational fractional bandwidth of both antennas, 28.6 % and 34.7 %, respectively. Both two antennas exhibit high RE values at the center of their operational bands, respectively, 92% and 98%. And their corresponding realized gain values are ~8 and ~3 dBi, respectively. The electrical sizes of the two antennas are *ka* = 2.4 and 1.74, respectively.

B. Operating Modes

To explain the mechanisms that lead to the radiation characteristics of both antennas, Fig. 3 displays the operating modes; the *E*-field distributions in the *zox*-plane that is centered between the radiation patches and feed structures; and the 3D radiation patterns of both antennas. Fig. 3(a) illustrates that the *E*-field distribution of the MSA at its lower resonance frequency, 3.8 GHz, resembles the TM_{10} mode of a patch antenna. Due to the interaction between the slot on the ground plane and the gap between the patches in the center of the metasurface, the *E*-field orientation over the ground slot is anti-parallel to that at the gap at the higher resonance frequency, 4.5 GHz. Therefore, the corresponding *E*-field distribution between the radiating patches and the ground plane resembles the antiphase TM_{20} mode rather than the standard TM_{20} mode. Note that the latter would deteriorate the uniformity of the radiation patterns [13], [19].

The design of the NFRP dipole antenna yields the same basic behaviors as those of the MSA except for the patterns, principally because there is no ground plane. Fig. 3(b) shows that the *E*-field near the NFRP patches at the lower resonant frequency, 3.8 GHz, resembles the fundamental electric dipole mode [19]. Interestingly, similar to the antiphase TM_{20} mode of the MSA, the surface current orientations of the feed strip and the NFRP patches are also reversed at the higher resonant frequency, 4.5 GHz. This due to the series and shunt capacitances that arise from the center gap and between the patches and the dipole, respectively. As a result, the NFRP patches operate in the antiphase 2nd dipole mode and, hence, widen the operational bandwidth and yield uniform radiation patterns. In contrast, the standard 2nd dipole mode also would seriously deteriorate the uniformity of the radiation patterns as illustrated.

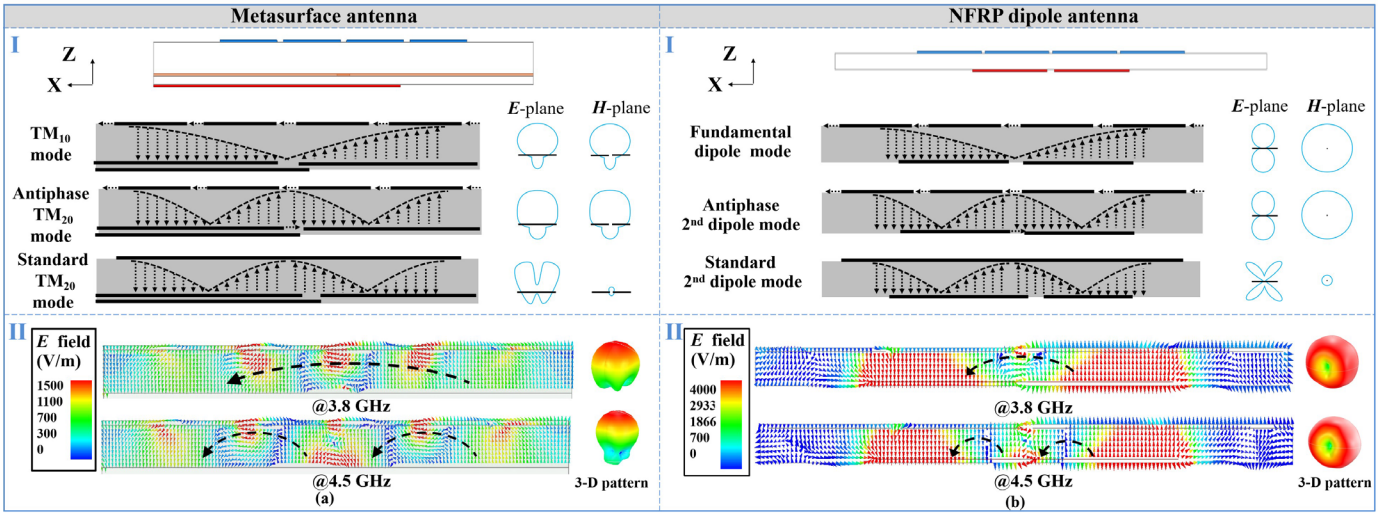

Fig.3. Illustrations of the operating mechanisms of the (a) slot-driven MSA and (b) dipole-driven NFRP antenna. (I) Theoretical sketch and radiation patterns of the corresponding operational modes. (II) Simulated *E*-field distributions in the center *zox*-plane and the 3-D radiation patterns at the two resonance frequencies.

The equivalent circuit model of the NFRP dipole antenna shown in Fig. 4 was developed to attain a better understanding of its operating mechanisms. The driven element is represented with the classical dipole circuit elements proposed in [20]. The NFRP element portion of the circuit model consists of four pairs of elements, i.e., a resistance R_p and an inductance L_p that represent each of its four patches. The three capacitors, C_p, represent the capacitances introduced by the gaps between the patches. The capacitors, C_m, represent the couplings between the driven element and each of the patches. The radiation resistance corresponding to the radiated power is R_{rad}. As Fig. 4 illustrates, the $|S_{11}|$ results from the equivalent circuit model agree very well with those obtained from the simulations of the actual antenna.

C. Further Miniaturization

To attain an ESA with similar performance characteristics, an interdigitated NFRP structure with a thinner Rogers RO4003C substrate was developed. Interdigitated structures, also called interdigitated capacitors (IDCs), can increase the series capacitance values, C_p, between adjacent patches [21]-[23]. Moreover, a lower antenna profile increases the coupling capacitance, C_m, values between driven and NFRP elements of the system. These two aspects of the equivalent circuit model established that the desired miniaturization could be accomplished.

Fig. 5 illustrates the evolution of the IDC-based NFRP dipole antenna. The initial design is the patch-based dipole antenna. The IDC structure in generation II and III contains five fingers. The simulated $|S_{11}|$ and realized gain values of each generation are displayed in Fig. 5. Going from Ant. I to Ant. III, higher series C_p and coupling C_m capacitances are achieved physically by introducing the fingers of the IDC-based NFRP element, increasing their length, and lowering the substrate thickness. Moreover, two strips are introduced on each end of the driven dipole to facilitate good impedance matching. The height of the substrate and the width and length of the driven dipole provide fine tuning. The two resonance frequencies associated with each generation decrease significantly as noted in the subplots. Note that although the gaps of the driven dipole and the NFRP structure are not aligned exactly in generations II and III, the coupling mechanisms and the field distributions are consistent with the initial design. Thus, they produce similar uniform radiation patterns. The electrical size of the final generation, Ant. III, is electrically small with ka = 0.987. The final bandwidth is ~ 2.5 times larger than that of a NFRP ESA with the same electrical size [24] as shown in Fig. 5(c). Moreover, the antennas maintain symmetric dipole radiation patterns, stable realized gain values, and high radiation efficiency during the evolution of all three cases.

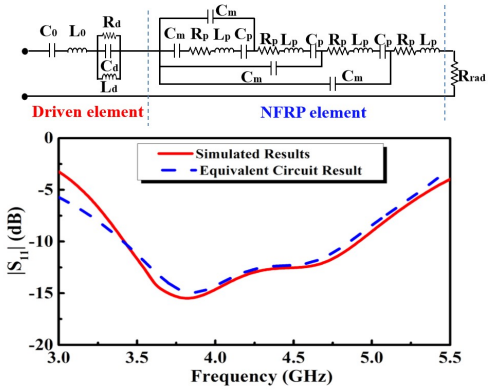

Fig. 4. Equivalent circuit model (top) and its $|S_{11}|$ values compared to those of the actual gap-excited NFRP dipole antenna (bottom). Circuit model parameters: C_0 = 0.45 pF, L_0 = 1.75 nH, R_d = 185 Ω, L_d = 0.1 nH, C_d = 8.16 pF, R_p = 14 Ω, L_p = 2 nH, C_p = 1 pF, C_m = 1.1 pF, and R_{rad} = 39 Ω.

III. Optimized Prototype and Measured Results

While all of the designs in Fig. 5 were obtained with idealized HFSS lumped ports, Ant. III was further optimized by fine tuning L_2 and W_2 to take into the account of the presence of the coaxial cable and balun present in the measurements. A prototype of this optimized design was then fabricated, assembled and tested. Its geometry and design parameters are given in Fig. 6 and in Table I, respectively. As shown in Fig. 6, the IDC-based NFRP element and the exciting top-hat loaded dipole element are printed on opposite sides of the Rogers RO4003C substrate. The inner and outer conductors of a KTG 086-50 semi-rigid cable were soldered at the center of the two strips of the exciting dipole. The pieces of the prototype and the assembled version as the antenna under test (AUT) in the measurement chamber are shown in Figs. 7(a) and (b), respectively. A sleeve balun with a 31mm length and 3 mm radius was employed in the measurements simply to eliminate the influence of the leakage currents on the outer wall of the chamber's long cable [25]. The $|S_{11}|$ values were measured with an Agilent E8361A Vector Network Analyzer.

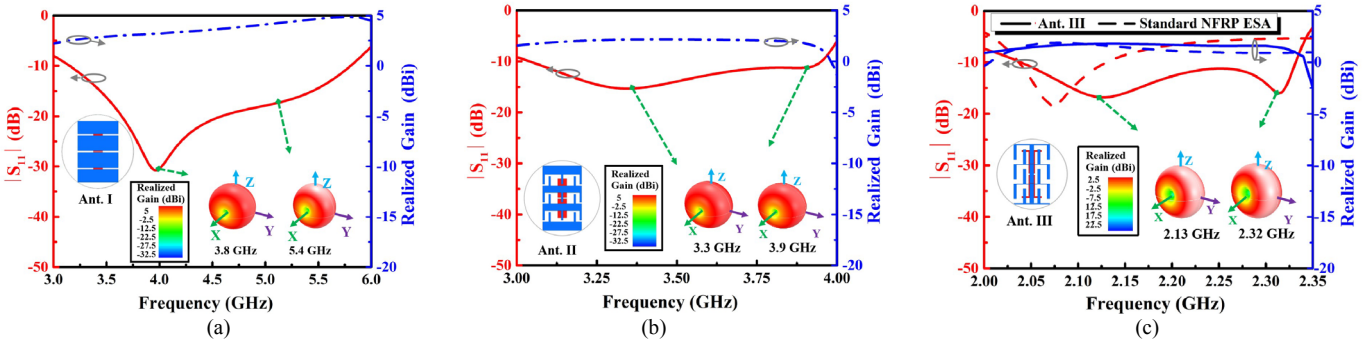

Fig. 5. The simulated $|S_{11}|$ and realized gain values as functions of the source frequency of the evolution of the IDC-based NFRP dipole antenna. The 3-D radiation patterns correspond to the indicated resonance frequencies. (a) Ant. I with no fingers and 0.6 mm substrate thickness. (b) Ant. II with 5.8 mm finger lengths and 0.4 mm substrate thickness. (c) Ant. III with 11.5 mm finger lengths and 0.203 mm substrate thickness and comparison NFRP ESA from [24].

As shown in Fig. 8(a), the measured (simulated) $|S_{11}|$ results indicate that the antenna exhibits a wide –10-dB impedance bandwidth from 2.05 to 2.37 GHz (2.044 to 2.36 GHz) with the corresponding fractional bandwidth of 14.4% (14.3%). The total electrical size of the antenna at the lower bound of its operational bandwidth was ka = 0.987.

The far-field radiation performance was measured in an anechoic chamber at the National Key Laboratory of Science and Technology on Communications, University of Electronic Science and Technology of China, Chengdu, China. As shown in Fig. 8(b), the measured (simulated) peak realized gain values are quite stable ~1.4 dBi (~1.5 dBi) within the operational band. Moreover, the RE values were higher than ~85% (~95%) over the entire operational bandwidth. Fig. 9 presents the measured and simulated realized gain patterns at its two resonant frequencies. Due to fabrication errors and measurement issues, the gain at boresight witnessed a ~1.5 dBi decrease, as seen in Fig. 8(b). Nonetheless, stable peak radiation results and uniform patterns were achieved over its entire operational band. Overall, the measured values are in agreement with their simulated ones.

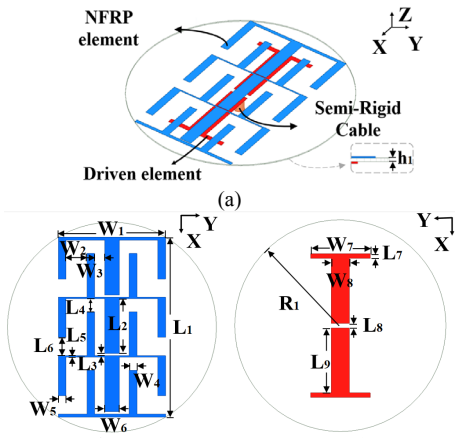

Fig. 6. Geometry of the optimized IDC-based NFRP dipole ESA. (a) 3D view. (b) Top view of the IDC NFRP element. (c) Bottom view of the exciting top-hat loaded dipole.

TABLE I. DIMENSIONS OF THE OPTIMIZED IDC-BASED NFRP ESA (UNIT: MILLIMETERS)

h_1=0.203	L_1=39.48	L_2=12	L_3=0.5	L_4 = 2.9
L_5=0.3	L_6=4.0	L_7=1.0	L_8=1.0	L_9=14.1
R_1=23	W_1=23.6	W_2=4.6	W_3=2.2	W_4=1.7
W_5=1.7	W_6=3.2	W_7=13	W_8=4.0	null

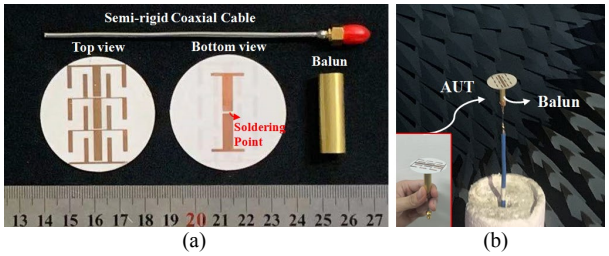

Fig. 7. Fabricated IDC-based NFRP dipole ESA prototype. (a) Antenna's components before assembly. (b) AUT in the anechoic chamber.

This electric ESA's simulated quality factor Q; Chu lower bound $Q_{Chu} = 1/(ka)^3 + 1/(ka)$, and Q-ratio: $Q_{ratio} = Q/[RE\times(1.5Q_{Chu})]$, are 4.63, 2.05, and 1.77 respectively [1], [26],[27]. Its maximum directivity is D_{max} = 1.72 dBi. The corresponding directivity-Q ratio: D_{max}/Q = 0.367, is near the upper bound for this planar antenna: 0.84 $(ka)^3$ = 0.807 [28]. Compared to the reference NFRP antenna with Q = 12.82, Q_{ratio} = 4.38, and D_{max}/Q = 0.134 [24], the optimized prototype has a much lower Q value (larger bandwidth) and higher directivity-bandwidth product.

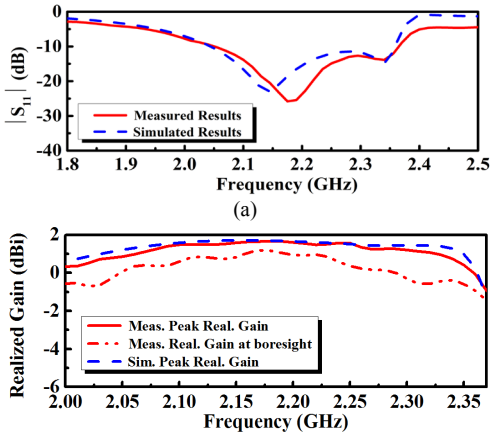

Fig. 8. Measured and simulated results of the prototype antenna as functions of the source frequency. (a) $|S_{11}|$ values. (b) Realized gain values.

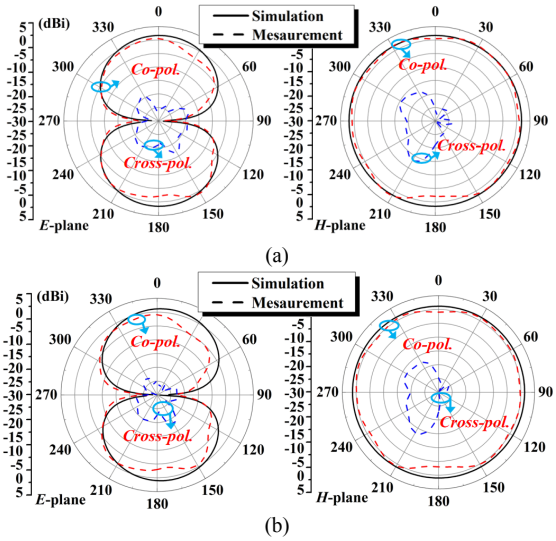

Fig. 9. Prototype's measured (simulated) realized gain patterns. (a) At the lower resonance frequency, 2.18 (2.14) GHz. (b) At the higher resonance frequency, 2.35 (2.35) GHz.

IV. CONCLUSION

A wideband, electrically small NFRP dipole antenna was presented. Benefiting from the large capacitance it introduces and the antiphase 2nd dipole mode it facilitates, the IDC-based NFRP element reduced the electric length, broadened the impedance bandwidth, and maintained the uniform radiation behavior over the entire operational band. The measured results, in good agreement with their simulated values, demonstrated that the prototype has a 14.4% fractional impedance bandwidth, which is ~2.5 times wider in comparison to a NFRP ESA with the same electrical size. Our antenna is attractive for many wideband and space- limited applications, such as satellite communication systems, wireless local area

networks, and radio frequency identification (RFID) applications.

REFERENCES

[1] L. J. Chu, "Physical limitations of omnidirectional antennas," *J. Appl. Phys.*, vol. 19, pp. 1163–1175, 1948.

[2] R. W. Ziolkowski and A. Erentok, "Metamaterial-based efficient electrically small antennas," *IEEE Trans. Antennas Propag.*, vol. 54, no. 7, pp. 1516–1529, Jul. 2006.

[3] A. Erentok and R. W. Ziolkowski, "Metamaterial-inspired efficient electrically small antennas," *IEEE Trans. Antennas Propag.*, vol. 56, no. 3, pp. 691–707, Mar. 2008.

[4] R. W. Ziolkowski, P. Jin, and C.-C. Lin, "Metamaterial-inspired engineering of antennas," *Proc. IEEE*, vol. 99, no. 10, pp. 1720–1731, Oct. 2011.

[5] M.-C. Tang and R. W. Ziolkowski, "Efficient, high directivity, large front-to-back-ratio, electrically small, near-field-resonant-parasitic antenna," *IEEE Access*, vol. 1, no. 1, pp. 16–28, May 2013.

[6] P. Jin, C.-C. Lin, and R. W. Ziolkowski, "Multifunctional, electrically small, planar near-field resonant parasitic antennas," *IEEE Antennas Wireless Propag. Lett.*, vol. 11, pp. 200–204, 2012.

[7] M.-C. Tang, R. W. Ziolkowski, S. Xiao, and M. Li, "A high-directivity, wideband, efficient, electrically small antenna system," *IEEE Trans. Antennas Propag.*, vol. 62, no. 12, pp. 6541-6547, Dec. 2014.

[8] M.-C. Tang, B. Y. Zhou, Y. Duan, X. Chen and R. W. Ziolkowski, "Pattern-reconfigurable, flexible, wideband, directive, electrically small near-field resonant parasitic antenna," *IEEE Trans. Antennas Propag.*, vol. 66, no. 5, pp. 2271-2280, May 2018.

[9] M.-C. Tang, X. Chen, M. Li, and R. W. Ziolkowski, "Particle swarm optimized, 3-D-printed, wideband, compact hemispherical antenna," *IEEE Antennas Wireless Propag. Lett.*, vol. 17, no. 11, pp. 2031–2035, Nov. 2018.

[10] N. Zhu and R. W. Ziolkowski, "Active metamaterial-inspired broad-bandwidth, efficient, electrically small antennas," *IEEE Antennas Wireless Propag. Lett.*, vol. 10, pp. 1582–1585, 2011.

[11] M.-C. Tang, N. Zhu, and R. W. Ziolkowski, "Augmenting a modified Egyptian axe dipole antenna with non-Foster elements to enlarge its directivity bandwidth," *IEEE Antennas Wireless Propag. Lett.*, vol. 12, pp. 421–424, 2013.

[12] W. Liu, Z. N. Chen, and X. Qing, "Metamaterial-based low-profile broadband mushroom antenna," *IEEE Trans. Antennas Propag.*, vol. 62, no. 3, pp. 1165–1172, Mar. 2014.

[13] W. Liu, Z. N. Chen, and X. Qing, "Metamaterial-based low-profile broadband aperture-coupled grid-slotted patch antenna," *IEEE Trans. Antennas Propag.*, vol. 63, no. 7, pp. 3325–3329, Jul. 2015.

[14] Z. Wu, X. Chen, and K. Li, "Dual-band antenna integrating with rectangular mushroom-like superstrate for WLAN applications," *IEEE Antennas Wireless Propag. Lett.*, vol. 15, pp. 1269–1272, 2015.

[15] W. Sun, Y. Li, Z. Zhang, and Z. Feng, "Broadband and low-profile microstrip antenna using strip-slot hybrid structure," *IEEE Trans Antennas Propag.*, vol. 16, pp. 3118–3121, 2017.

[16] W. E. I. Liu, Z. N. Chen, X. Qing, J. Shi, and F. H. Lin, "Miniaturized wideband metasurface antennas," *IEEE Trans. Antennas Propag.*, vol. 65, no. 12, pp. 7345–7349, Dec. 2017.

[17] F. H. Lin and Z. N. Chen, "A method of suppressing higher order modes for improving radiation performance of metasurface multiport antennas using characteristic mode analysis," *IEEE Trans. Antennas Propag.*, vol. 66, no. 4, pp. 1894–1902, Apr. 2018.

[18] W. Che, W. Ma, W. Peng, and Z. Chen, "Bandwidth-enhanced electrically large microstrip antenna loaded with SRR structures," *IEEE Antennas Wireless Propag. Lett.*, vol. 18, no. 4, pp. 576–580, Apr. 2019.

[19] C. A. Balanis, *Antenna Theory: Analysis and Design*, 3rd. Hoboken, NJ, USA: Wiley Interscience, 2005.

[20] M. Hamid and R. Hamid, "Equivalent circuit of dipole antenna of arbitrary length," *IEEE Trans. Antennas Propag.*, vol. 45, no. 11, pp. 1695-1696, Nov. 1997.

[21] S. Sun, L. Zhu, and H.-H. Tan, "A compact wideband bandpass filter using transversal resonator and asymmetrical interdigital coupled lines," *IEEE Mircow. Wireless Compon. Lett.*, vol. 18, no. 3, pp. 173–175, Mar. 2008.

[22] Y. Juan, W. Che, Z. N. Chen, and W. Yeng, "A longitudinally compact Yagi-Uda antenna with a parasitic interdigital strip," *IEEE Antennas Wireless Propag. Lett.*, vol. 16, pp. 2618–2621, 2017.

[23] A. Lai, T. Itoh, and C. Caloz, "Composite right/left-handed transmission line metamaterials," *IEEE Microw. Mag.*, vol. 5, iss. 3, pp. 34–50, Sept. 2004.

[24] P. Jin and R. W. Ziolkowski, "High-directivity, electrically small, low-profile near-field resonant parasitic antennas," *IEEE Antennas Wireless Propag. Lett.*, vol. 11, pp. 305–309, 2012.

[25] C. Icheln, J. Krogerus, and P. Vainikainen, "Use of balun chokes in small-antenna radiation measurements," *IEEE Trans. Instrum. Meas.*, vol. 53, no. 2, pp. 498–506, Apr. 2004.

[26] H. L. Thal, "New radiation limits for spherical wire antennas," *IEEE Trans. Antennas Propag.*, vol. 54, no. 10, pp. 2757–2763, Oct. 2006.

[27] S. R. Best, "Low Q electrically small linear and elliptical polarized spherical dipole antennas," *IEEE Trans. Antennas Propag.*, vol.53,pp. 1047–1053, Mar. 2005.

[28] M. Gustafsson, C. Sohl, and G. Kristensson, "Illustrations on new physical bounds on linearly polarized antennas," *IEEE Trans. Antennas Propag.*, vol. 57, no. 5, pp. 1319–1327, May 2009.